Noninvasive photoacoustic imaging of the thoracic cavity and the kidney in small and large animals

Kwang Hyun Song and Lihong V. Wang[a]
Optical Imaging Laboratory, Department of Biomedical Engineering, Washington University in St. Louis, Campus Box 1097, One Brookings Drive, St. Louis, Missouri 63130-4899

The internal organs of rats and rabbits were clearly imaged noninvasively using a deeply penetrating reflection-mode photoacoustic imaging system. This imaging system had previously been found to provide an imaging depth limit of ~38 mm. In the thoracic cavity, major blood vessels connecting to the heart were imaged, and the right atrium was imaged as deeply as ~8 mm. In the abdominal cavities, the kidney and vena cava inferior were also imaged *in situ*. The vena cava inferior ~13.7 mm deep was imaged. The kidney of a New Zealand white rabbit was also imaged. This study shows the deep internal organ imaging capability of the system in animals. This technology can potentially be used to study tumors in internal organs, and be adapted to clinical diagnosis. © *2008 American Association of Physicists in Medicine.* [DOI: 10.1118/1.2977534]

I. INTRODUCTION

The need for noninvasive small animal imaging is rapidly growing, as it becomes a standard method to study tumor growth and monitor tumor regression during therapy. It is also useful in the development of clinical treatments. Magnetic resonance imaging (MRI), computed tomography (CT), and positron emission tomography (PET) are currently the main radiological methods. They have been adapted for small animal imaging from clinical technologies.[1,2] With their scaled down adaptation, these imaging modalities have better spatial resolution and sensitivity than their clinical versions. However, MRI still has several orders of magnitude less sensitivity than optical methods to exogenous contrast agents, CT has less sensitivity to soft tissue and uses potentially harmful radiation, and PET uses radioactive isotopes.[3] These drawbacks limit repeated use. Optical modalities, such as fluorescence imaging and diffuse optical tomography, are safe, inexpensive, nonionizing, and highly sensitive to endogenous optical contrast, such as hemoglobin, as well as to exogenous contrast agents. Furthermore, optical methods are capable of functional imaging of such as the concentration and oxygen saturation of hemoglobin.[4–6] Purely optical imaging, however, has poor spatial resolution due to the overwhelming optical scattering effect in deep regions of soft tissues.

Photoacoustic (PA) imaging is an emerging hybrid technology: It overcomes the poor spatial resolution of purely optical imaging methods, but retains optical sensitivity and specificity as well as ultrasonic imaging depth scalability.[7–9] PA imaging forms an image by detecting the ultrasonic waves generated in soft tissues. When a short pulsed laser light illuminates the tissues, absorbed optical energy in absorbers causes thermoelastic expansion of the absorbers, generating ultrasonic waves. Therefore, this technology can provide high ultrasonic resolution and good imaging depth, both of which are scalable with the ultrasonic frequency.[10,11] Furthermore, since PA waves are generated by local optical absorption, the technology enjoys the advantages of optical imaging modalities—sensitivity and specificity to optical contrast. With these fundamental advantages, PA imaging technology has been applied to various areas, such as tumor angiogenesis studies,[12] skin cancer detection,[13] functional brain studies,[14,15] and human breast cancer imaging.[16] Particularly in small animal studies, it has produced remarkable brain cortex images with functional and molecular contrasts.[17]

Dark-field PA microscopy was developed in reflection mode, which allows more versatility in imaging.[10,18] This imaging system has produced high-resolution vasculature images as well as oxygen saturation (SO_2) maps within ~3 mm depth below the skin surface in animals.[18] An optical detection based PA imaging system was developed and showed good morphological images *in situ*.[19] Even though both studies made great progress, their imaging depth did not exceed ~3 mm, and they were not appropriate for internal organ imaging since they employed high frequency ultrasonic detectors and low optical excitation energy.

Thus, a deep reflection-mode PA imaging system was proposed using lower frequency ultrasonic detectors and higher optical energy in the deeply penetrating near-infrared (NIR) spectral region, while the laser fluence is still within the ANSI safety limit.[11,20] This study demonstrated the potential for imaging structures embedded ~30 mm below the surface of chicken breast tissue (absorption coefficient μ_a =0.1 cm^{-1} and reduced scattering coefficient μ_s'=2.0 cm^{-1})[21] and imaging a rat spleen. Despite both depth capability of the system and feasibility of internal organ imaging in the study, internal organ imaging is still thought to be problematic because many organs have either strong optical absorption limiting light propagation or gas cavities preventing ultrasound transmission. Depending on their depth,
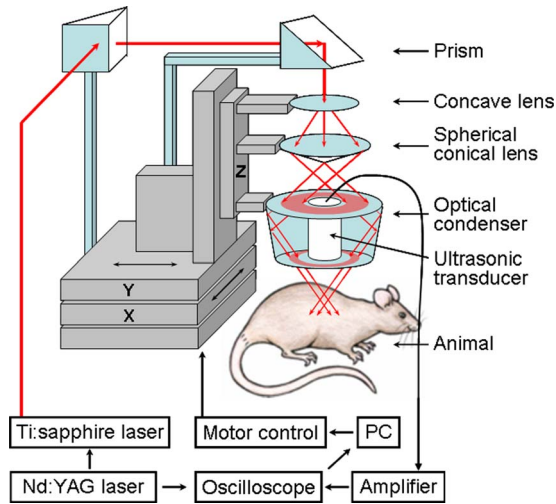
FIG. 1. Schematic of the reflection-mode photoacoustic imaging system.

location, configuration, and absorption, however, many organs can still be imaged, including their internal structures.

In this study we imaged various anatomical structures in the thoracic cavity and the cervix of a rat. The kidney and other structures in the abdominal cavities of both a rat and a rabbit were also imaged. We believe that this work lays a foundation for studying internal organs using PA imaging in small animals.

II. METHODS AND MATERIAL

II.A. Photoacoustic system

The PA imaging system for internal organs was designed in reflection mode (Fig. 1). This imaging system employed ring-shaped dark-field instead of bright-field illumination. This illumination can achieve efficient detection of PA waves from deep regions by reducing the generation of PA waves on the surface. The surface signals can otherwise interfere with those from deeper regions and obscure their detection.[10] The system can also improve homogeneity of optical fluence by illuminating an object from more directions. Thus, it can reduce the shadow effect caused by an adjacent shallower absorptive object. Three optical parts, a concave lens (LC2873-B, Thorlabs), a spherical conical lens (cone angle: 135.6°), and an optical condenser (angles: 76°, 104°) adjustable on an optical rail, produced this illumination pattern. The distances between the optical components are ~7 and ~12 cm, respectively. To achieve stronger PA waves in deep regions, we delivered high optical energy to the targeted region while observing the ANSI safety limit.[20] Therefore, two prisms mounted on an XY linear translation stage were used instead of a single optical fiber, which has a lower damage threshold.

To image internal organs, including embedded structures, we chose a NIR 800 nm optical wavelength to achieve deeper optical penetration for all applications in this study. Light at this wavelength is close to the isosbestic point of the molar extinction spectra of oxy- and deoxy-hemoglobin, i.e., it is sensitive to the concentration of hemoglobin and insen-sitive to the oxygenation of blood. The light source was a tunable Ti:sapphire laser (LT-2211A, LOTIS TII) pumped by a Q-switched Nd:YAG laser (LS-2137/2, LOTIS TII). Light pulses from this laser have a <15 ns pulse duration and a 10 Hz pulse-repetition rate. The light was sufficiently broadened to conform to the ANSI safety limit for the skin at this wavelength (illumination area: ~2 cm^2, distance to the skin surface: ~7 mm, fluence limit: 31 mJ/cm^2).[20]

For the PA signal detection with minimal ultrasonic attenuation, we chose a 5 MHz central frequency ultrasonic transducer (V308, Panametrics-NDT). The transducer is spherically focused with 2.54 cm focal length, 1.91 cm diameter active element, and 72% bandwidth based on the full width at half maximum amplitude. The f number (focal length/diameter of active element) is 1.33. The 5 MHz transducer was suited for achieving good transverse resolution since it has a low f number (high numerical aperture). Transverse resolution was estimated by $1.02\lambda f/d$ (λ is the measured wavelength, f is the focal length, and d is the diameter of the active element). An object was situated below a 5 cm $\times$ 5 cm opening in the bottom of the water container, and the opening was sealed with a thin and clear membrane. To couple the object and the transducer acoustically, the transducer was immersed in water, then ultrasonic gel (Sonotech, Inc.) was applied between the membrane and the object. The transducer scanned the object through the opening. The spatial resolutions of this system with the 5 MHz ultrasonic transducer at 19 mm deep were ~144 μm in the axial direction and ~560 μm in the transverse direction.[11]

To obtain 3D PA data, we employed raster scanning of a focused ultrasonic transducer using an XY linear translation stage (XY-6060, Danaher Motion), controlled by a computer. To shorten data-acquisition time, continuous scanning, synchronized with a data-acquisition system without signal averaging, was employed. The scanning step sizes for a 1D scan (X direction, B scan) and a 2D scan (XY directions, 3D image) were ~0.2 and ~0.4 mm, respectively. Those step sizes were adjusted mostly according to the targeted field of view and acquisition time. For instance, with 0.2 and 0.3 mm step sizes and a 10 Hz pulse-repetition-frequency laser system, the acquisition time was ~14 s for the B scan and ~15 min for the 3D image, covering a 20 mm $\times$ 20 mm surface area.

PA signals received by the ultrasonic transducer were first amplified by an amplifier (5072PR, Panametrics-NDT) and then digitized by an oscilloscope (TDS 5054, Tektronix) with a 50 MHz sampling rate. These PA signals were compensated for the laser energy fluctuations from pulse to pulse by signals from a photodiode (DET110, Thorlabs), which measured the energy of each laser pulse.

An image was formed by compiling multiple A scans. At a single position, the transducer received the PA signal that originated along the depth direction (Z direction), which is called an A scan. This A scan was converted into a 1D depth-resolved image by multiplying the time by the speed of sound in soft tissues ($\approx$1500 m/s). With scanning in the X direction, a 2D B-scan image was formed. Through addi-

tional Y-directional scanning, a 3D image was obtained. To visualize 3D data, maximum amplitude projection (MAP) was employed, where the maximum amplitude value in each A scan is projected onto an XY imaging plane.[18]

II.B. Animal preparation and drug information

All animal experiments were carried out in compliance with the guidelines on the care and the use of laboratory animals at Washington University in St. Louis. For small animal experiments, adult Sprague Dawley rats weighing 200–350 g were used. The rat was initially anesthetized with a mixture of ketamine (85 mg/kg) and xylazine (15 mg/kg) for the hair removal procedure. Since hair scatters laser light, the hair on the region of interest was gently removed using a commercial hair-removal lotion before imaging. Before an *in situ* imaging experiment, the animal was euthanized by a pentobarbital overdose (0.1 ml of 26% concentration). For an *in vivo* experiment, anesthesia was maintained using a vaporized isoflurane gas system (1 L/min oxygen and 0.75% isoflurane, Euthanex Corp.) during all image acquisitions. Vitals (arterial SO$_2$ and heart rate) were monitored using a pulse oximeter (NONIN Medical Inc., 8600V). For hydration, 8 ml of 0.9% saline was administered. After image acquisitions, the animal was euthanized by pentobarbital overdose. To verify the structures in the PA image, the animal was dissected and photographed. For a larger animal experiment, a freshly sacrificed New Zealand white rabbit weighing ~3 kg was used. Hair on the region of interest was removed with the same method as for the small animal.

III. RESULTS

III.A. Noninvasive photoacoustic imaging of a rat thoracic cavity *in situ*

We imaged the anatomical features in the thoracic cavity and cervix of a rat weighing ~200 g. The 5 MHz central frequency ultrasonic transducer was employed. The rat was laid down supine on the animal holder [Fig. 2(a)]. After 3D data were acquired, a PA image was constructed in the form of MAP in the coronal direction [Fig. 2(b)]. The major blood vessels, such as the common carotid artery (CA), jugular vein (JV), superior vena cava, and left cranical vena cava were clearly imaged. The right atrium (RA) and the heart (HT) were also imaged. Figure 2(c) is the corresponding anatomical photograph of the thoracic cavity taken after obtaining the PA image. Anatomical photographs [Fig. 2(d)] show the left subclavian vein, external jugular vein, JV, and common CA. Figure 2(e) is a photograph of the rib cage, showing the blood vessels around the sternum. The PA MAP image and the anatomical photographs match well. The B scans [Fig. 2(f)], corresponding to the dashed lines (a, b, c, and d) in Fig. 2(b), show the depths of the structures. For instance, the JV is located at ~5 mm, and the RA is situated at ~8 mm [Figs. 2(d)(a) and 2(d)(c)]. Skin contours were heuristically added along the skin surfaces for depth measurement since the PA signals from the skin surfaces were too weak to be detected by software due to the use of dark-field
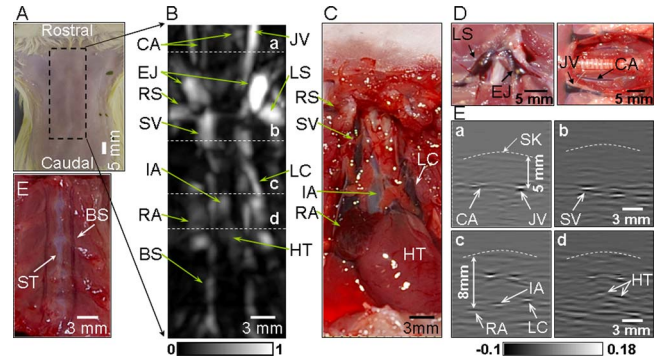
FIG. 2. (A) Photograph of the chest of a rat with hair removed before photoacoustic imaging. Dotted lines indicate the imaging region. (B) Coronal photoacoustic MAP image of the thoracic cavity and the cervical area. (C) Corresponding anatomical photograph of the thoracic cavity. (D) Anatomical photographs of cervical area. (E) Blood vessels inside the rib cage. (F) B-scan images corresponding to the dotted lines (a, b, c, and d) in (B). BS, blood vessels around the sternum; CA, common carotid artery; EJ, external jugular veins; HT, heart; IA, innominate artery; JV, jugular vein; LS, left subclavian vein; LC, left cranial vena cava; RA, right atrium; RS, right subclavian vein; ST, sternum; and SV, superior vena cava.

illumination and 800 nm wavelength of laser. In the B-scan images, dark–bright–dark patterns are shown around blood vessels since the detected PA waves from cylindrical sources, such as blood vessels, were biopolar signals. Synthetic-aperture focusing and coherence weighting were applied to improve the transverse resolution and SNR in the out-of-focus zone of the ultrasonic transducer.[22] This technique also slightly flattened blood vessels in the image. In PA imaging, we experienced optical and acoustic attenuation along the depth direction, hence, deeper structures were imaged with weaker signal and were not visualized in a MAP image. To make the deep structures (RA, IA, and HT) more visible, therefore, time gain compensation was applied to the depth-resolved A scans based on the diffusion theory (effective attenuation coefficient $\mu_{\text{eff}} = 1.54$ cm^{-1}), where we considered only optical attenuation for simplicity.

III.B. Noninvasive photoacoustic imaging of a rat kidney *in situ* and *ex vivo*

Kidneys remove wastes from the blood stream, excrete them, and maintain homeostasis (electrolyte concentrations, control of blood volume, and regulation of blood pressure).[23] We imaged *in situ* the kidney of a rat weighing ~205 g with the same system parameters as used in the thoracic cavity imaging. The rat was laid down sideways on the holder as shown in Fig. 3(a). The region of imaging is marked with dotted lines. When intervening structures are located closer to the transducer than the targeted region and generate stronger PA signals, the targeted region is blocked in the MAP image. In the kidney image, the rib cage and liver partially covered the kidney. In the MAP image, therefore, some details of the kidney were concealed by the rib cage and liver. Thus, for the MAP image formation, the 3D data were divided into two parts in the depth direction at the top surface of the kidney. First, the PA signals from above the kidney were used to form a saggital MAP image of the liver (LV)
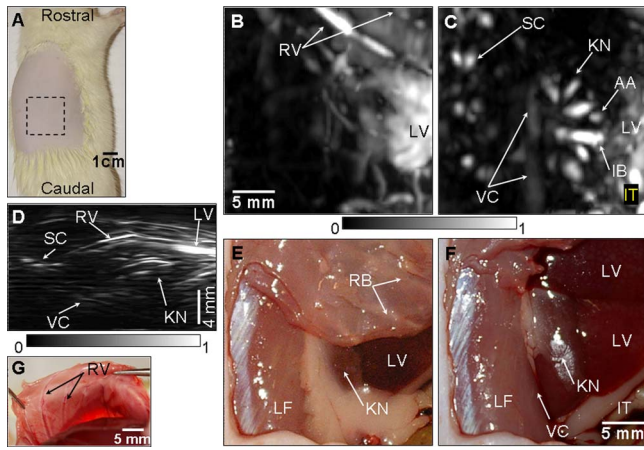
FIG. 3. Noninvasive *in situ* photoacoustic image of the right kidney of a rat. (A) Photograph of the rat before photoacoustic imaging. (B) Saggital photoacoustic MAP image of the blood vessels around the ribs and the liver. (C) Saggital photoacoustic MAP image of the kidney, the vena cava inferior, and the spinal cord. (D) Axial photoacoustic MAP image showing the depths of the structures. (E) Anatomical photograph with the ribs intact, but the skin removed. (F) Anatomical photograph with the skin and the ribs removed. (G) Anatomical photograph showing blood vessels (RV) around ribs (taken from the inside). The photographs and photoacoustic images were obtained from the right side of the rat. AA, arcuate blood vessels; IB, interlobar blood vessels; IT, intestines; KN, kidney; LF, lumbodorsal fascia; LV, liver; RV, blood vessels around ribs; SC, blood vessels in the spinal cord; and VC, vena cava inferior.

and the blood vessels (RV) around the ribs [Fig. 3(b)]. Second, the PA signals from below the top surface of the kidney were processed to construct a saggital MAP image [Fig. 3(c)], showing the interlobar (IB) and arcuate (AA) blood vessels in the kidney (KN),[23] the spinal cord (SC), and the vena cava inferior (VC). Figures 3(e) and 3(f) are the corresponding anatomical photographs. In Fig. 3(f), the rib cage and fatty tissue were removed to reveal the kidney and the liver more clearly. The LV and the RV in Fig. 3(b) are in good agreement with those in Figs. 3(e) and 3(g). The KN, LV, and the intestine (IT) in Fig. 3(c) match those in Fig. 3(f). The blood vessel in the SC[24] and the vena cava inferior (VC) are not shown in the two anatomical photographs because they are concealed by the lumbodorsal fascia and the KN. To improve the visibility of deeper structures in the images, time gain compensation was applied to the depth-resolved A scans with the same effective attenuation coefficient as the previous thorax imaging. This compensation improved the visibility of the vena cava inferior (VC), situated ~13.7 mm deep. Overall depths of each structure are shown in the axial MAP image [Fig. 3(d)]. To confirm the embedded structures of the kidney, it was excised and then imaged *ex vivo*. The IB and AA blood vessels[23] were imaged in Fig. 4(a), and are in good agreement with those in the *in situ* kidney image [Fig. 3(c)]. In particular, the interlobular (IU) blood vessels,[23] which are smaller than others, were also imaged in the *ex vivo* kidney image [Fig. 4(a)]. Figures 4(b) and 4(c) are photographs of the excised and further bisected kidney, respectively.
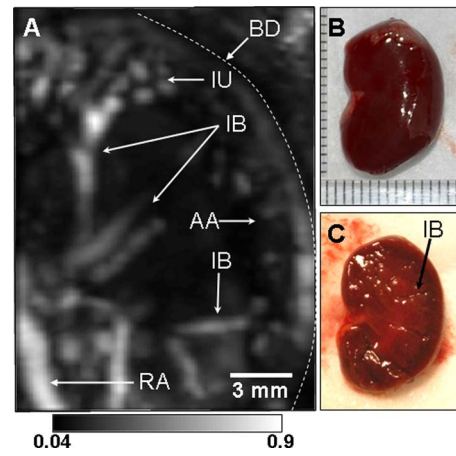
FIG. 4. (A) *Ex vivo* photoacoustic saggital MAP image of an excised whole rat kidney. (B) Photograph of the excised kidney. (C) Photograph of the bisected kidney. AA, arcuate blood vessels; IB, interlobar blood vessels; IU, interlobular blood vessels; RV, renal blood vessels; and BD, boundary of the kidney.

III.C. Photoacoustic imaging of a rabbit kidney *in situ*

We imaged the kidney of a New Zealand white rabbit weighing ~3 kg. The 5 MHz central-frequency ultrasonic transducer was employed. A PA image was acquired with the skin intact post mortem. Figure 5(a) shows a saggital MAP image of the KN, a blood vessel in the muscle (BV), and the IT. Figure 5(b) is the corresponding anatomical photograph, which shows the kidney and the intestine. The structures in the PA image match those in the anatomical photograph well. Unlike the *in situ* kidney image of a rat [Fig. 3(c)], this image does not show the embedded structures of the kidney.
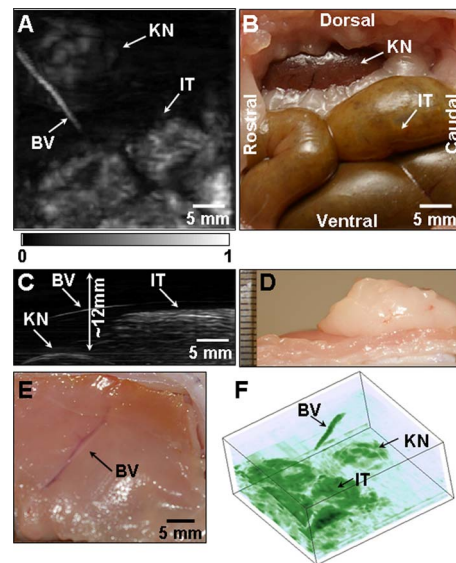
FIG. 5. Noninvasive *in situ* photoacoustic image of the left kidney of a rabbit. (A) Saggital photoacoustic MAP image. (B) Corresponding anatomical photograph. (C) Axial photoacoustic MAP image. (D) Photograph showing the thickness of tissue layers situated above the kidney. (E) Photograph of the blood vessel (BV) in the skin (taken from the inside). (F) Volume rendered image. The photographs and PA images were obtained from the left side of the rabbit. BV, blood vessel; IT, intestine; KN, kidney surface.

Figure 5(c) is an axial MAP image, indicating the depths of the structures. The skin surface was not shown in Fig. 5(c) since a relatively high-contrast structure (IT) suppresses a low-contrast structure (skin). The top surface of the kidney was as deep as ~12 mm below the skin surface. The intestine and the blood vessel near the kidney were seated ~6 mm deep. Figure 5(d) confirmed the depth of the kidney, and Fig. 5(e) is an anatomical photograph showing the blood vessel (taken from the inside). Figure 5(f) was the volume rendered 3D image.

IV. DISCUSSION

In this study, for the first time to our knowledge, the thoracic cavity, cervical area, and kidneys of small and large animals were imaged using the deeply penetrating reflection-mode PA imaging. However, several limitations exist in this study: the small window between the ribs for the thoracic cavity imaging, limited optical penetration depth in highly absorptive tissues, and a relatively long scanning time. As shown in the thoracic cavity image [Figs. 2(b) and 2(d)], PA signals could be detected from only part of the heart. The heart was caged by the ribs and sternum, and this imaging system employs raster scanning of a single ultrasonic transducer. Thus, the PA signals from the heart and other structures were blocked by the ribs and sternum, and as a result, the transducer received the PA signals through the small windows between the ribs. An ultrasonic array system might be the solution for the small window limitation since it can be tilted easily as in medical cardiac ultrasonography. With such a system, PA imaging can be made more versatile, enabling an efficient assessment of morphological changes in blood vessels, such as the common carotid artery, jugular vein, left cranial vena cava, and superior vena cava. Furthermore, PA imaging can also image functions such as oxygen saturation (SO$_2$)[14,18] and blood volume.[15]

The left external jugular vein and left cranial vena cava (LS) show higher contrast than the ones on the right-hand side. The contrast difference was caused by the position difference of blood vessels in the region of acceptance angle of the transducer (Z direction). Since the focused ultrasonic transducer was employed, when an object was in off-focus zone, which is defined as −6 dB width of a pressure profile, the PA amplitude of the object had to be at least twice lower than in the focal zone. Normalization methods considering a pressure profile of a transducer may be required to meet this challenge.

In the in situ rabbit kidney imaging (Fig. 5), the internal structures were not revealed. The suspected reason is the limited optical penetration. Since the optical fluence (~15 mJ/cm^2) used for these experiments was under the ANSI safety limit (fluence limit: 31 mJ/cm^2), increasing optical fluence within the safety limit can enhance the SNR. In addition, the skin and muscle of the rabbit in the abdomen were much thicker than those in a rat (>5 mm). Thus, there was more optical attenuation. In this study, to shorten the acquisition time, PA signals were not averaged. With a real-time ultrasonic array system, signal averaging will be avail-

able while a reasonable frame rate is maintained, and will improve the imaging depth. In kidney imaging, animal positioning is another consideration since a kidney is surrounded by liver and intestine. Improperly positioning an animal can conceal a kidney in PA imaging.

The breathing motion will be another challenge in in vivo organ imaging, limiting clear structural visualization. The breathing motion irregularly changes the positions of internal organs, causing image distortion. These changes are not easily predictable. Possible solutions might again be an ultrasonic array system with breathing gating. In addition, using a high-pulse-repetition frequency laser, an array-based PA system can potentially reach the frame rate of clinical ultrasonography. Employing an ultrasonic array system can also enable the coregistration of a PA image with an ultrasonic image, potentially providing more morphological and functional information of organs.

In conclusion, we successfully imaged small animal vasculatures in the thoracic cavity and the cervical area of a rat. Also, the internal structures of the kidney in a rat were clearly imaged. This technique was then applied to a larger animal, a rabbit, to image the abdominal cavity. In addition to morphological imaging, PA imaging can potentially image functional hemodynamics, such as hemoglobin concentration and oxygen saturation with the use of multiple wavelengths of laser light. With these morphological and functional capabilities, cancer detection, assessment of cancer treatment, monitoring of cancer-related physiological events, etc., can be potential applications of PA imaging in the clinic.

a)Author to whom correspondence should be addressed. Electronic mail: lhwang@biomed.wustl.edu

[1] T. F. Massoud and S. S. Gambhir, "Molecular imaging in living subjects: Seeing fundamental biological processes in a new light," Fusion Eng. Des. 17, 545–580 (2003).

[2] R. Weissleder, "Scaling down imaging: Molecular mapping of cancer in mice," Nat. Rev. Cancer 2, 11–18 (2002).

[3] M. Yang et al., "Whole-body optical imaging of green fluorescent protein-expressing tumors and metastases," Proc. Natl. Acad. Sci. U.S.A. 97, 1206–1211 (2000).

[4] D. A. Benaron et al., "Noninvasive functional imaging of human brain using light," J. Cereb. Blood Flow Metab. 20, 469–477 (2000).

[5] J. E. Brazy et al., "Noninvasive monitoring of cerebral oxygenation in preterm infants: Preliminary observations," Pediatrics 75, 217–225 (1985).

[6] B. Chance et al., "A novel method for fast imaging of brain function, non-invasively, with light," Opt. Express 2, 411–423 (1998).

[7] C. G. A. Hoelen et al., "Three-dimensional photoacoustic imaging of blood vessels in tissue," Opt. Lett. 23, 648–650 (1998).

[8] R. A. Kruger et al., "Thermoacoustic computed tomography using a conventional linear transducer array," Med. Phys. 30, 856–860 (2003).

[9] V. Ntziachristos et al., "Looking and listening to light: The evolution of whole-body photonic imaging," Nat. Biotechnol. 23, 313–320 (2005).

[10] K. Maslov, G. Stoica, and L. V. Wang, "In vivo dark-field reflection-mode photoacoustic microscopy," Opt. Lett. 30, 625–627 (2005).

[11] K. H. Song and L. V. Wang, "Deep reflection-mode photoacoustic imaging of biological tissue," J. Biomed. Opt. 12, 060503 (2007).

[12] G. Ku et al., "Imaging of tumor angiogenesis in rat brains in vivo by

photoacoustic tomography," Appl. Opt. **44**, 770–775 (2005).

[13] J. T. Oh *et al.*, "Three-dimensional imaging of skin melanoma in vivo by dual-wavelength photoacoustic microscopy," J. Biomed. Opt. **11**, 34032 (2006).

[14] X. Wang *et al.*, "Noninvasive laser-induced photoacoustic tomography for structural and functional in vivo imaging of the brain," Nat. Biotechnol. **21**, 803–806 (2003).

[15] E. W. Stein, K. Maslov, and L. V. Wang, "Noninvasive mapping of the electrically stimulated mouse brain using photoacoustic microscopy," Proc. SPIE **6856**, 685654 (2008).

[16] S. Manohar *et al.*, "Initial results of in vivo non-invasive cancer imaging in the human breast using near-infrared photoacoustics," Opt. Express **15**, 12277–12285 (2007).

[17] M.-L. Li *et al.*, "Simultaneous molecular and hypoxia imaging of brain tumors in vivo using spectroscopic photoacoustic tomography," Proc. IEEE **96**, 481–489 (2007).

[18] H. F. Zhang *et al.*, "Functional photoacoustic microscopy for high-resolution and noninvasive in vivo imaging," Nat. Biotechnol. **24**, 848–851 (2006).

[19] E. Z. Zhang, L. Jan, and B. Paul, "Three dimensional photoacoustic imaging of vascular anatomy in small animals using an optical detection system," Proc. SPIE **6437**, 64370S (2007).

[20] American National Standards, "American National Standard for the Safe Use of Lasers," ANSI Z136.1-2000, New York, 2000.

[21] G. Marquez *et al.*, "Anisotropy in the absorption and scattering spectra of chicken breast tissue," Appl. Phys. Lett. **37**, 798–804 (1998).

[22] M. L. Li *et al.*, "Improved in vivo photoacoustic microscopy based on a virtual-detector concept," Opt. Lett. **31**, 474–476 (2006).

[23] A. C. Guyton and J. E. Hall, *Textbook of Medical Physiology*, 10th ed. (Saunders, Pennsylvania, 2000).

[24] E. C. Greene, *Anatomy of the Rat*, Vol. 27 (Hafner, New York, 1963).